Journal of Zhejiang University-SCIENCE A 2025 26(10):1010-1020
www.jzus.zju.edu.cn; www.springer.com/journal/11582
E-mail: jzus_a@zju.edu.cn

Research Article
https://doi.org/10.1631/jzus.A2400503

Check for updates

Electrostatic potential distribution image-transfer learning method for highly accurate prediction of lithium diffusion barriers on transition metal dichalcogenide surfaces

Jian CHEN[1,2], Yao KANG[1,2], Xudong WANG[1,2], Hao HUANG[1], Man YAO[1,2]✉

[1]*School of Materials Science and Engineering, Dalian University of Technology, Dalian 116024, China*
[2]*Key Laboratory of Solidification Control and Digital Preparation Technology (Liaoning Province), Dalian University of Technology, Dalian 116024, China*

Abstract: Calculating the inter-layer ion diffusion barrier, a crucial metric for evaluating the rate performance of 2D electrode materials, is time-consuming using the transition state search approach. A novel electrostatic potential distribution image (EPDI) transfer learning method has been proposed to efficiently and accurately predict the lithium diffusion barriers on metal element-doped transition metal dichalcogenide (TMD) surfaces. Through the analysis of the mean electrostatic potential (MEP) around binding sites, a positive correlation between binding energy and MEP in VIB-TMDs was identified. Subsequently, transfer learning techniques were used to develop a DenseNet121-TL model for establishing a more accurate mapping between the binding energy and electrostatic potential distribution. Trained on training sets containing 33% and 50% transition state search calculation results, which save 66% and 50% of the calculation time, respectively, the model achieves accurate predictions of the saddle point binding energy with mean absolute errors (MAEs) of 0.0444 and 0.0287 eV on the testing set. Based on the prediction of saddle point binding energies, we obtained a diffusion minimum energy profile with an MAE of 0.0235 eV. Furthermore, by analyzing the diffusion data, we observed that the diffusion barrier was lowered by 10% on V-doped TiS_2 compared to the stoichiometric surface. Our findings are expected to provide new insights for the high-throughput calculation of ion diffusion on 2D materials.

Key words: Transition metal dichalcogenide (TMD); Deep learning; Transfer learning; Electrostatic potential; Lithium-diffusion

1 Introduction

A vast range of 2D materials have been widely used in energy storage systems, due to their unique physical and chemical properties compared to their bulk counterparts (Shao et al., 2019; Wu and Yu, 2019; Bahari et al., 2021; Theerthagiri et al., 2021, 2022a, 2022b). To enhance the performance of 2D materials, modification engineering has been extensively explored, including element doping (Lee et al., 2021; Wang XG et al., 2021; Wang RH et al., 2022), defect engineering (Liu HP et al., 2020; Zhang et al., 2020; Liu and Fan, 2023), and surface functional group modification (Giebeler and Balach, 2021; Zhang et al., 2021). Applying these various modification methods to 2D materials can expand the scope of exploratory material research. However, conventional experimental approaches and discrete Fourier transform (DFT) calculations cannot keep pace with the rapidly increasing demands in the study of 2D materials. Therefore, using high-throughput DFT calculations and machine learning presents an exciting opportunity for efficient screening of the 2D materials space. Machine learning has emerged as a valuable tool to aid in high-throughput DFT calculations for predicting the properties of 2D materials (Zhan et al., 2019; Das et al., 2020; Kang et al., 2021; Ryu et al., 2022). As an advanced subfield of machine learning, deep learning exhibits enhanced feature extraction capabilities compared to conventional machine learning. It has been leveraged to analyze multidimensional raw data for screening the properties of 2D materials. Some researchers have

✉ Man YAO, yaoman@dlut.edu.cn
Man YAO, https://orcid.org/0000-0002-7322-9258

Received Oct. 24, 2024; Revision accepted Jan. 16, 2025;
Crosschecked Sept. 5, 2025

constructed new deep neural networks tailored to their research tasks (Dong et al., 2021; Leist et al., 2022). Using existing deep neural networks or transfer learning techniques has also yielded notable advancements in predicting the properties of 2D materials (Dong et al., 2019; Masubuchi et al., 2020).

The electrochemical properties of 2D materials determine the performance of the electrode. Machine learning has been implemented to predict these properties in the search for high-performance electrode materials. First, regarding discharge capacity, Wang GY et al. (2021) constructed a dataset containing the reported discharge capacities of 168 doped lithium nickel-cobalt-manganese (NCM) systems and used six regression machine learning models to predict the discharge capacity. Due to the limited size of the experimental dataset, the prediction accuracy of the above models is insufficient. Besides, the complexity of the electrochemical process results in intricate nonlinear relationships between electrochemical performance and various fundamental physical parameters. Consequently, the associated datasets exhibit high-dimensional characteristics, complicating the optimization of model hyperparameters (Sendek et al., 2017; Wang et al., 2017; Liu Y et al., 2020). One approach to addressing the issue of small datasets is to use existing online databases. For example, based on the Computational 2D Materials Database (C2DB), Haastrup et al. (2018) and Kabiraj and Mahapatra (2022) selected four descriptors (binding energy, root mean square (RMS) displacement, percentage of area change, and charge transfer) to evaluate lithium storage capacity, mechanical sturdiness, and interaction strength between lithium atoms and substrates. Subsequently, crystal graph convolutional neural network and MEGNet models were developed to predict these four descriptors (Xie and Grossman, 2018; Chen et al., 2019; Kabiraj and Mahapatra, 2022). In another example, the voltage of electrodes for multivalent metal-ion batteries was accurately predicted by an interpretable deep learning model obtained through transfer learning techniques applied to the crystal graph convolutional neural network (Zhang et al., 2022). Moreover, Chaney et al. (2021) used a clusterwise linear regression machine learning model to predict the absorption energy of lithium on Janus Mo/WXY (X, Y=S, Se, Te). However, the prediction of ion diffusion performance, which plays a significant role in electrode properties, has rarely been efficient for 2D materials using machine learning. The time-consuming nature of transition state search has presented a challenge in enabling high-throughput calculations of diffusion barriers.

Here, we propose a new deep learning-based method that accurately predicts the diffusion barriers of lithium ion on the surfaces of metal element-doped transition metal dichalcogenides (TMDs) using transfer learning techniques. The developed algorithm consists of three essential sections: extraction of surface electrostatic potential distribution images, prediction of the lithium binding energies on the saddle and valley points of the surface energy profile, and transformation of binding energy to the diffusion barrier. Firstly, considering the Coulomb interaction between lithium atoms and the surface, we hypothesized that the distribution of surface electrostatic potential significantly influences the binding energy. Therefore, we obtained a batch of 1328 fragment images representing the surface electrostatic potential distribution at valley and saddle points along the lithium diffusion path. Through area integration of the fragment images, the mean electrostatic potential (MEP) was obtained and a strong positive linear relationship between MEP and binding energy for VIB-TMDs was observed, thus validating our previous conjecture. Secondly, to establish a more accurate and comprehensive mapping, we used transfer learning techniques to construct a deep neural network capable of predicting the binding energy with a mean absolute error (MAE) of 0.0287 eV. Thirdly, the diffusion barriers were calculated in batches based on the difference in binding energy between the valley and saddle points. Successive diffusion barriers were then merged to obtain the minimum diffusion path energy profile according to the diffusion path. In summary, compared to traditional machine learning, the electrostatic potential distribution image (EPDI) method based on the convolutional neural network model does not require the design of complex high-dimensional feature vectors. Moreover, due to the efficient extraction of potential energy surface features of surface electrostatic potential by the convolutional neural network, this method achieves a higher prediction accuracy for diffusion barriers than those reported in the literature (Ahmed et al., 2020; Chang et al., 2021; Lu et al., 2023). The algorithm provides new insights into predicting diffusion barriers and expands the approach of high-throughput calculation of diffusion barriers for 2D materials.

2 Methods

2.1 First-principles calculation

All density functional theory calculations in this study were performed using the projector augmented wave method (PAW) (Blöchl, 1994) implemented in the Vienna ab initio Simulation Package (VASP) (Kresse and Furthmüller, 1996). The Perdew-Burke-Ernzerhof generalized gradient approximation (PBE-GGA) (Langreth and Mehl, 1983; Perdew et al., 1996) was used to describe the exchange-correlation energy. van der Waals interactions were estimated using the DFT-D3 method proposed by Grimme et al. (2010). A plane wave basis set with an energy cutoff of 500 eV was used. The unit cell and 3×3×1 supercell configurations used 8×8×1 and 2×2×1 gamma central Monkhorst-Pack grids, respectively. The maximum residual force after structure relaxation was set to 0.02 eV/Å for each atom, and the electronic relaxation convergence threshold was set to 1×10^{-5} eV. To break the periodicity in the *z*-direction for free surfaces, a vacuum region of 15 Å was included. To obtain the minimum energy path, the climbing image nudged elastic band (CINEB) method was used (Henkelman and Jónsson, 2000). The isosurface level for the electrostatic potential distribution on metal-doped TMD monolayer surfaces was set to 0.01 ebohr^{-3}. The lithium diffusion barriers on the stoichiometric surface of the TMDs are consistent with the findings of previous studies (Table S1 of the electronic supplementary materials (ESM)). The MEP is obtained by area integration using a Python program.

2.2 Dataset construction

We initially doped the monolayer surfaces of TMDs such as MoS_2, $MoSe_2$, WS_2, WSe_2, HfS_2, $HfSe_2$, TiS_2, ZrS_2, NbS_2, TaS_2, VS_2, and VSe_2 with metal heteroatoms (Al, Co, Cr, Cu, Fe, Mn, Ni, V, and Zn), resulting in a total of 106 surface configurations. Additionally, ab initio calculations were performed to determine the sdurface electrostatic potential distributions of 6×6×1 supercell configurations. The corresponding electrostatic potential distribution images were generated using VESTA software (Momma and Izumi, 2011) (Fig. S1 of the ESM). Furthermore, considering the interaction of lithium atoms with the surface at valley and saddle points along the diffusion path, a Python code was developed to extract valley point (vp) and saddle point (sp) local images from the 106 electrostatic potential distribution images, resulting in a total of 4554 images. Since the crystal exhibits periodicity and the structure around the dopant atom has central symmetry, the 4554 fragment images contain duplicates that can be obtained by rotating or flipping. After removing the duplicates, 1328 distinct fragment images were obtained, comprising 701 vp fragments and 627 sp fragments.

Subsequently, the minimum energy profiles of the lithium diffusion path for metal-doped TMD surfaces were calculated using the first-principles calculation with the CINEB method. Moreover, through the calculation of the binding energy for a lithium atom at the valley point (marked as E_{b_vp}) and saddle points (marked as E_{b_sp}), label pairs consisting of vp image (E_{b_vp}) and sp image (E_{b_sp}) were established. Finally, we assigned all the label pairs of vp image (E_{b_vp}) and different proportions (0%, 17%, 33%, and 50%) of the label pairs of sp image (E_{b_sp}) to construct the training/validation set, while the remaining label pairs of sp image (E_{b_sp}) were allocated to the testing set to evaluate the performance of the training model.

2.3 Model and tools settings

The VGG19 (Simonyan and Zisserman, 2014), ResNet34/101/152 (He et al., 2016), and DenseNet121/169 (Huang et al., 2017) model architectures were used. These models were implemented using the PyTorch framework (Paszke et al., 2019). The outputs of these models were adjusted to one output. The weights and hyperparameters of the pre-trained models were optimized using 5-fold cross-validation, with a learning rate of 0.00005 and a total of 3000 epochs. The batch sizes of the training, validation, and testing sets were set to 40, 16, and 16, respectively. Data augmentation techniques were used to generate additional training data and enhance the generalization capability of the model.

3 Results and discussion

3.1 Mean electrostatic potential

To efficiently predict the lithium diffusion barrier on the surface, it is necessary to substitute the computationally time-consuming diffusion barrier with a fast-calculated physical quantity. Through the analysis of the electron localization function (ELF) of lithium absorption on metal-doped MoS_2 with various elements

(Al, Fe, Cu, Cr, Co, Zn, V, Ni, Mn), we observed that the ELF value between lithium atoms and sulfur atoms was close to 0, indicating a weak chemical interaction during lithium absorption (Fig. S1). Consequently, the strength of Li–S bonds depends on the Coulomb interaction between the lithium and sulfur atoms, while the interaction between the lithium atom and the surface is governed mainly by the electrostatic potential distribution. Hence, we aimed to use the characteristics of the electrostatic potential distribution to predict the lithium diffusion barrier.

We speculated that the electrostatic potential is related to the adsorption energy of lithium and the surface. However, adsorption energy reflects only the energy difference between the stable states and does not account for the energy gap between the transition state and the stable state. To address this issue, we calculated the binding energy of the lithium atom at the transition state to include the information about the transition state, which is similar to the adsorption energy. Moreover, we attempted to predict the lithium binding energy based on the electrostatic potential and subsequently deduce the lithium diffusion barrier. In the following section, we outline the process for identifying the appropriate electrostatic potential distribution image in detail. At the valley points (vp) of the energy profile (Fig. 1), the lithium atom interacts mainly with three sulfur atoms, while at the saddle point (sp), two sulfur atoms form bonds with each lithium atom. Consequently, we hypothesized that the electrostatic potential distributions surrounding the lithium atom at the valley and saddle points have the most influence on the binding energies of the lithium atom. Therefore, the extraction of electrostatic potential images was performed based on the hexagonal unit cell of transition metal sulfides, as shown on the right side of Fig. 1a. Additionally, the diffusion barrier was calculated as the difference in binding energy between the valley and saddle points (E_{b_vp} and E_{b_sp}). The formula derivation is shown in Eqs. (S1)–(S4), which are included in the ESM.

To overcome the time-consuming nature of the transition state search calculation, our goal was to enable high-throughput computation of E_{b_sp} by establishing a mapping relationship between the surface electrostatic potential distributions and binding energies (which include all the E_{b_vp} and part of E_{b_sp}). Then, by the difference of E_{b_vp} and E_{b_sp}, the lithium diffusion

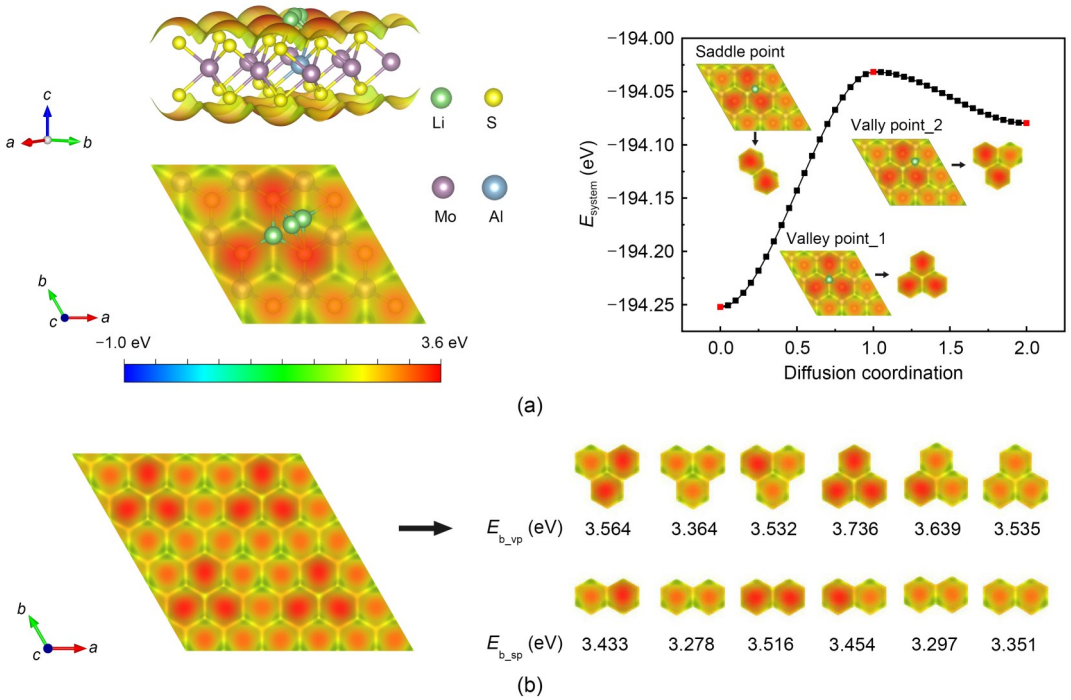

Fig. 1 Extraction process of valley points (vp) and saddle points (sp) of the surface electrostatic potential distribution: (a) lithium diffusion path and energy profile on the surface electrostatic potential distribution of Al-doped MoS_2 (the valley and saddle points are marked in red); (b) valley and saddle points on the surface electrostatic potential distribution of Al-doped MoS_2. References to color refer to the online version of this figure

barrier could be obtained. Fig. 1b shows a selection of clipped surface electrostatic potential distribution images for the supercell surface of Al-doped MoS_2. Furthermore, Fig. S2 illustrates 106 calculated surface electrostatic potential distribution images for the supercell surface of metal element-doped TMDs. To accurately batch clip these images, a Python program was developed to automate the process. Ultimately, 1328 surface electrostatic potential distribution images of the valley and saddle points were obtained, and subsequently, the corresponding 1328 E_{b_vp}/E_{b_sp} values for the lithium atom were calculated using first-principles calculations with the CINEB method.

Before establishing the mapping relationship, it is crucial to validate the aforementioned speculation regarding the strong correlation between the surface electrostatic potential distribution and the binding energy. To account for the Coulomb interaction between the lithium atom and the surface, the MEP was calculated as an indicator of the interaction strength. Furthermore, we used the Pearson correlation coefficient to assess the linear relationship between MEP and E_b (E_{b_vp} and E_{b_sp}). The Pearson correlation coefficient (R) is a numerical value ranging from −1 to 1 used to quantify the strength and direction of a linear relationship between two variables. A large absolute value of R indicates a strong linear correlation between E_b and MEP. Based on Fig. S2, we note that doping the same atom yields comparable surface electrostatic potential distributions. The Pearson correlation coefficient R(MEP, E_b) and the relationship between E_b and MEP for surfaces doped with the same atom in VIB-TMDs (MoS_2, $MoSe_2$, WS_2, WSe_2) are shown in Fig. 2. Significantly, the Pearson correlation coefficients R(MEP, E_{b_sp}) and R(MEP, E_{b_vp}) are consistently close to 0.95 and 0.90, respectively. These results indicate a robust positive linear relationship between E_b and MEP for surfaces doped with the same atom in VIB-TMDs.

Furthermore, to examine the strength of the positive linear correlation between E_b and MEP across various atom dopings, we combined the nine images from Fig. 2 into a singular image (Fig. 3a).

The data points were then visually distinguished by color, reflecting the increase in the valence electron numbers of the doped atoms. Remarkably, the data points exhibit an upward shift as the number of valence electrons (N_{ve}) of the doped atoms increases, with the exception of Al and V. Therefore, the number of valence electrons was used as a coefficient to adjust MEP (Fig. 3b). Significantly, except for Al and V, the Pearson correlation coefficient $R(N_{ve}\times\text{MEP}, E_b)$ was 0.94, indicating a robust positive linear correlation between E_b and the product of the number of valence electrons for the doped atoms and MEP. In conclusion, the electrostatic potential and binding energy show a strong linear correlation for VIB-TMD surfaces. However, in the case of IVB- and VB-TMD surfaces, a weak linear correlation exists between MEP and E_b. The variation of E_b with respect to MEP is shown in Figs. S3 and S4.

3.2 Transfer learning for diffusion barrier prediction

Based on the preceding discussion, the surface electrostatic potential significantly influences the strength of interaction between lithium atoms and the surface of VIB-TMDs. However, describing the interaction using MEP is not comprehensive for IVB- and VB-TMDs. Consequently, particular characteristics of surface electrostatic potential distributions affecting interactions were not considered in IVB- and VB-TMDs. To accurately and comprehensively extract the features of the surface electrostatic potential distribution that describe the interaction, we attempted to use a deep neural network with robust image feature extraction capabilities to address this challenge. However, designing and training a new deep neural network model with exceptional performance for our objective would be inefficient.

The transferability of deep neural networks is evident in their architecture: the front-end network serves as a task-agnostic feature extractor, while the backend network is closely aligned with the task at hand (Tan et al., 2018). Therefore, unlike rebuilding a deep neural network, transfer learning enhances the model's generalization ability and prediction accuracy, while also reducing the time required for parameter tuning (Yosinski et al., 2014; Tan et al., 2018). Thus, we aimed to use transfer learning techniques to establish our model for feature extraction of surface electrostatic potential distribution images. Consequently, the dataset was first built. Since the valley point binding energy calculation is efficient, all the valley point binding energies were added to the training set. Additionally, due to the time-consuming nature of calculating saddle point binding energies, half of these were used as the training set and the remaining half as the testing set (Fig. 4a).

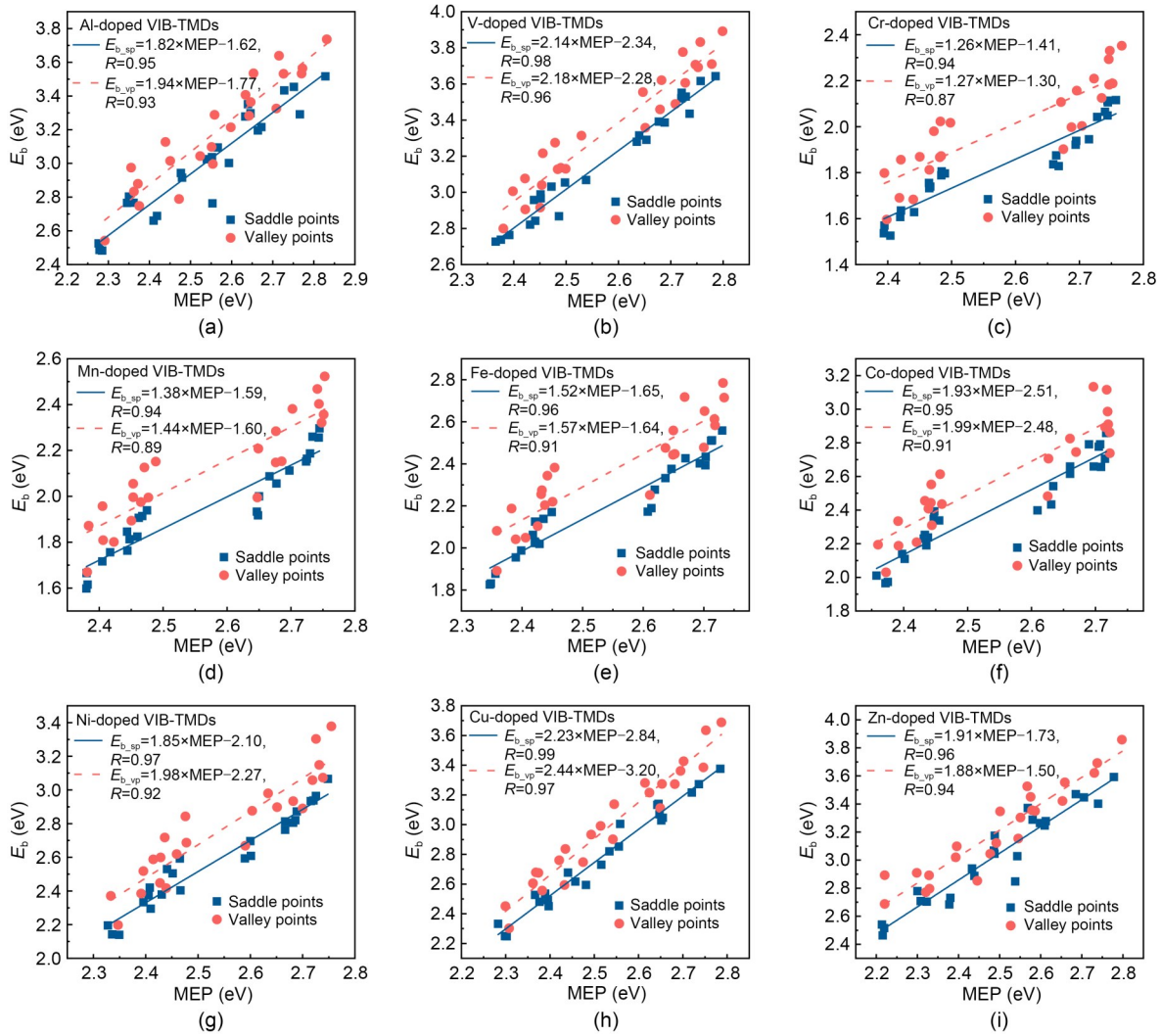

Fig. 2 Correlation between E_b of lithium atoms on metal element ((a) Al, (b) V, (c) Cr, (d) Mn, (e) Fe, (f) Co, (g) Ni, (h) Cu, and (i) Zn)-doped VIB-TMD surfaces and the MEP of saddle/valley points

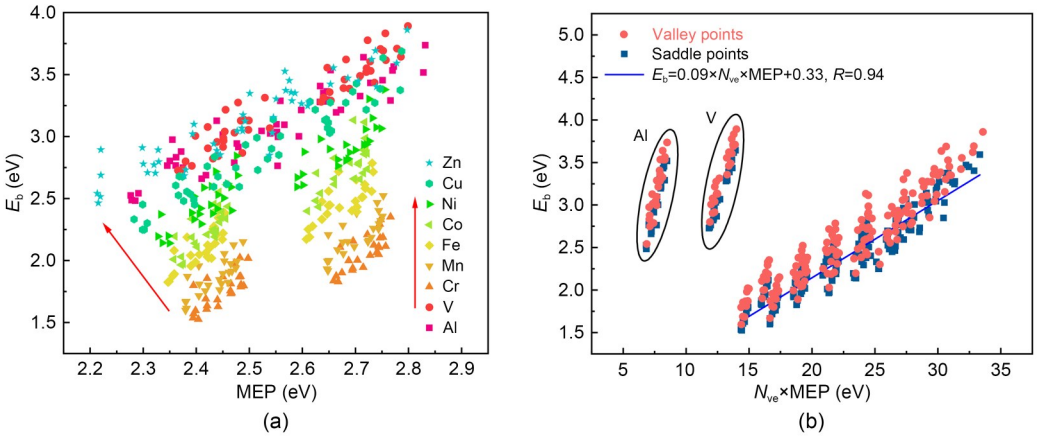

Fig. 3 Variation of E_b for lithium atoms on metal element-doped VIB-TMD surfaces with (a) MEP and (b) the product of the number of doped atom valence electrons and MEP of saddle/valley points. References to color refer to the online version of this figure

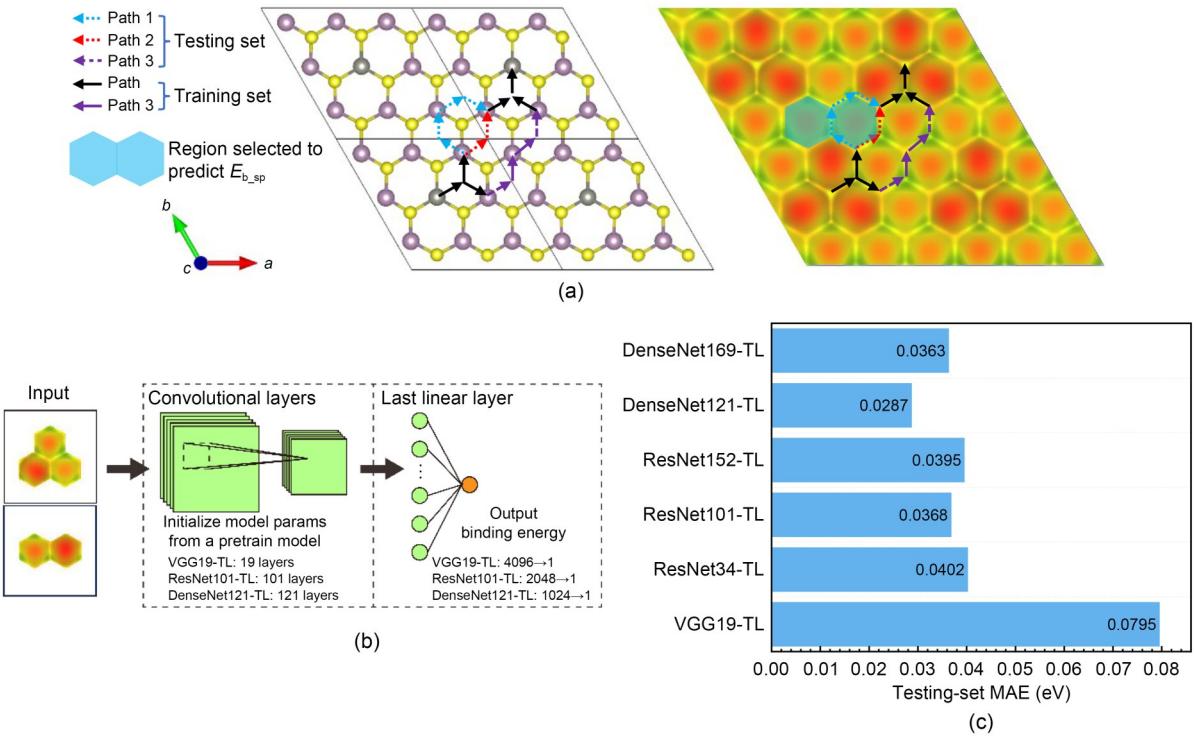

Fig. 4 (a) Three diffusion paths with different colors on the doped surface (left) and the corresponding surface electrostatic potential distribution (right) (the saddle point binding energy indicated by the dotted arrow serves as the test set, and that represented by the solid arrow serves as the training set); (b) Proposed approach of model-based transfer learning; (c) MAE of testing set of different models. References to color refer to the online version of this figure

Moreover, six established deep neural network architectures known for their robust image feature extraction capabilities were fine-tuned, namely VGG19-TL, ResNet34-TL, ResNet101-TL, ResNet152-TL, DenseNet121-TL, and DenseNet169-TL. Fig. 4b shows the model structures, wherein we retained the unchanged structure of the convolutional layers and adjusted the output of the last fully connected layer to 1. Subsequently, the input was the image depicting the local surface electrostatic potential distribution, with E_b specified as the output shown in Fig. 4b. Additionally, the model parameter was initialized using the pretrained models VGG, ResNet, and DenseNet, which had been trained on the ImageNet database. We performed 5-fold cross-validation to these models for 3000 epochs in which the MAE was set as the loss function. The MAEs of the testing set for the models with the best performance are shown in Fig. 4c. Note that the lowest MAE is 0.0287 eV for DenseNet121-TL. This MAE amounts to 0.81% of the average value (3.554 eV) for the saddle point binding energies in the testing set. This indicates that when half of the saddle point binding energies are used as the training set, the remaining half can be predicted with high accuracy. Additionally, Fig. S5 presents the performance of the best-performing models (VGG19-TL, ResNet101-TL, and DenseNet121-TL) on the testing set, along with the corresponding cumulative distribution functions of absolute errors. Furthermore, from the difference of E_{b_vp} and E_{b_sp}, a Python program was developed to convert the binding energies into diffusion barriers in batches, resulting in 318 energy profiles of the diffusion path. The Zn-doped MoS_2 surface was selected to showcase the prediction performance. Fig. S6 shows the energy profiles for the diffusion paths on the MoS_2 surface with the other metal atoms (Al, Cu, Co, Cr, Mn, Fe, Ni, and V). In Fig. 5b, all possible diffusion scenarios of the lithium atom on the Zn-doped MoS_2 surface are marked as blue, red, and purple arrows, and the overlapping sections of the three paths are highlighted in black.

The corresponding energy profiles of these paths are shown in Fig. 5a, in which the solid lines represent the energy profiles calculated using DFT and the dotted lines depict those predicted by DenseNet121-TL. The predicted values closely align with the dotted line,

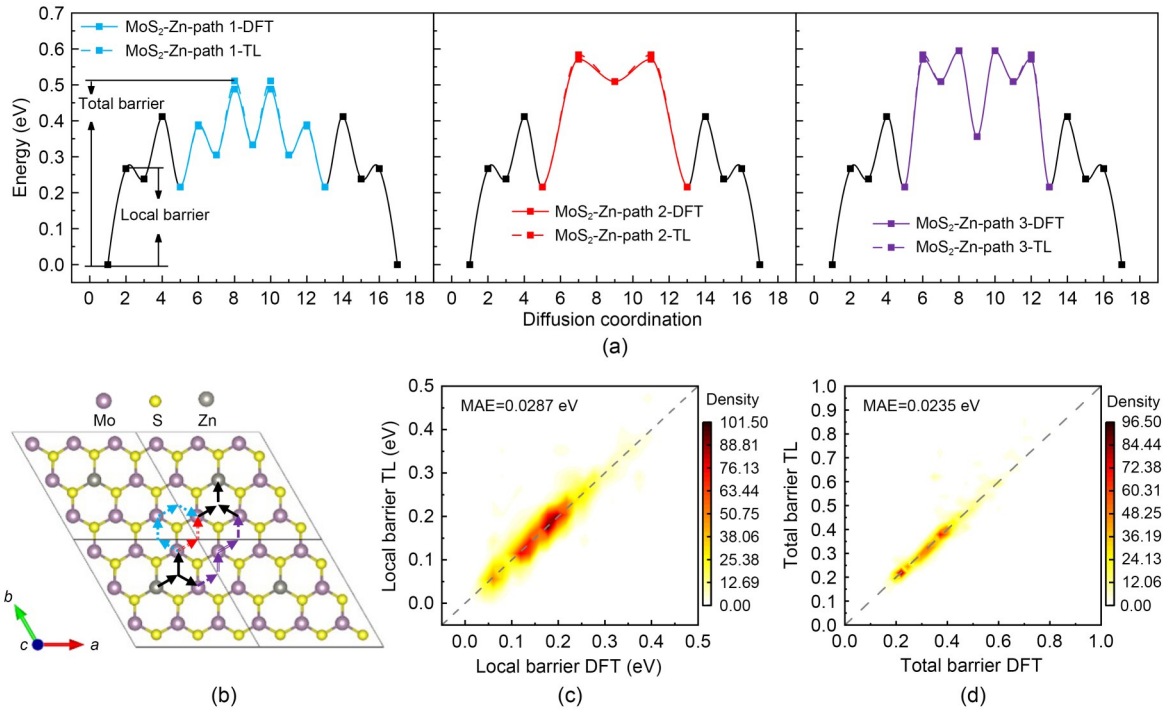

Fig. 5 Diffusion barrier prediction: (a) DFT calculation and DenseNet121-TL prediction values of energy profile for three lithium diffusion paths on a Zn-doped MoS_2 surface; (b) schematic diagram of three lithium diffusion paths on a Zn-doped MoS_2 surface; (c) parity plot of the DFT calculation and DenseNet121-TL prediction of the local lithium diffusion barrier on a Zn-doped MoS_2 surface; (d) parity plot of the DFT calculation and DenseNet121-TL prediction of the total lithium diffusion barrier on a Zn doped MoS_2 surface. References to color refer to the online version of this figure

indicating a high level of accuracy in the prediction of the potential barrier. Moreover, for the total metal-doped TMDs surfaces, we categorized the diffusion barriers into local and global diffusion barriers for discussion. A schematic saddle point binding energy prediction, as all valley point binding energies are calculated using DFT. The model shows improved prediction performance for global diffusion barriers, achieving an MAE of 0.0235 eV. This enhancement occurs because the global diffusion barrier is influenced by the local diffusion barrier calculated using DFT (Fig. 5d).

Although the DenseNet121-TL model shows excellent prediction performance on the testing set with half of the saddle point binding energies, significant time is still required for the transition state search calculations. Therefore, we aimed to reduce the proportion of saddle point binding energies in the training set to decrease the time spent on transition state search calculations while increasing the proportion of predicted saddle point binding energies. As mentioned above, the DenseNet121-TL exhibited the best performance among the deep learning models tested. Therefore, DenseNet121-TL was chosen to train on different training sets containing 0%, 17%, and 33% proportions of saddle point binding energies. The MAE and computation time for the first-principles calculations required to prepare the training set are shown in Fig. 6. As the amount of saddle point binding energies in the training set decreases, the model's predictive performance diminishes. Besides, when the proportion of CINEB calculation results in the training set is 1, it indicates that all results have been calculated using the DFT method.

Therefore, for the training set containing 33% saddle point binding energies, the MAE on the testing set is 0.0444 eV, which is still excellent for diffusion barrier prediction while saving nearly 70% of the calculation time compared to the conventional DFT methods. This prediction accuracy surpasses those of the following reported machine learning methods for diffusion barrier prediction: MAE of 0.048 eV for lithium diffusion in Li_3PO_4 (Li et al., 2017), MAE of 0.07/0.52 eV for copper diffusion through graphene/hBN (hexagonal boron nitride) (Ahmed et al., 2020), and root mean square error (RMSE) of 0.098 eV for hydrogen diffusion in alloys (Lu et al., 2023). Furthermore, when the training set does not include saddle point

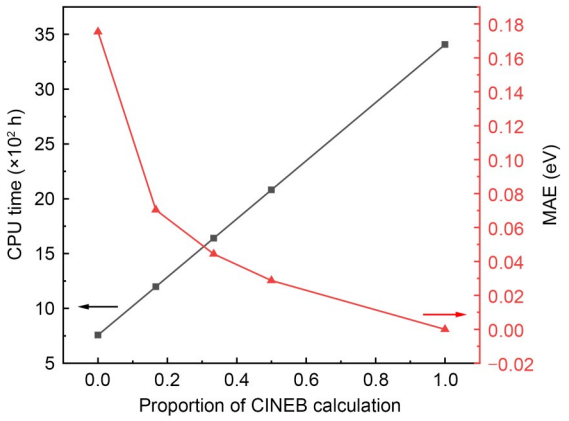

Fig. 6 Accuracy-efficiency trade-off of DenseNet121-TL under different dataset divisions, where all valley point binding energies and different proportions of saddle point binding energies were used as the training set, while the remaining saddle point binding energies comprised the testing set. The left vertical axis indicates the computation (CPU) time for first-principles calculations required to prepare the training set

binding energies, the MAE on the testing set, which contains all the saddle point binding energies, exceeds 0.16 eV, rendering it unacceptable for diffusion barrier prediction. In summary, this method requires us to provide a small number of saddle point binding energies to the model, enabling it to learn transition state information and enhance the prediction accuracy of diffusion barriers.

4 Conclusions

This paper presents a deep learning-based approach for predicting the lithium diffusion barrier on metal-doped TMD surfaces. Based on first-principles calculations, a dataset consisting of surface electrostatic potential images of valley and saddle points along the lithium diffusion path was constructed, with corresponding binding energies of lithium for metal-doped TMDs surfaces as labels. Furthermore, a strong positive correlation between the MEP of metal-doped VIB-TMD surfaces and the binding energies was observed. Additionally, to predict lithium diffusion barriers based on the differences in binding energies, several deep learning models were constructed using transfer learning techniques and the best model (DenseNet121-TL) was identified to establish a more accurate mapping between binding energy and electrostatic potential distribution. Trained on training sets containing 33% and 50% transition state search calculation results, the DenseNet121-TL model achieved MAEs of 0.0444 and 0.0287 eV on the testing set for saddle binding energy predictions, respectively. Moreover, the lithium diffusion minimum energy profiles on metal-doped TMD surfaces were obtained with an MAE of 0.0235 eV across 106 metal-doped TMD surfaces. Furthermore, by analysis of the diffusion barrier data, the diffusion barrier was reduced by 10% on V-doped TiS_2 compared to the stoichiometric surface. Our method enables the estimation of the complete lithium diffusion minimum energy profile by requiring only a small number of transition state search calculations. We expect that our work will facilitate high-throughput calculations of lithium diffusion barriers on 2D material surfaces.

Acknowledgments

This work is supported by the National Natural Science Foundation of China (Nos. 51974056 and 51474047), the Foundation of the Supercomputing Center of Dalian University of Technology, and the Foundation of the Key Laboratory of Solidification Control and Digital Preparation Technology (Liaoning Province), China.

Author contributions

Jian CHEN performed all the first-principles calculations, developed the algorithms based on the deep learning model, and wrote the manuscript. Yao KANG contributed to the establishment of the datasets. Xudong WANG and Hao HUANG helped with developing ideas. Man YAO helped with writing and data analysis.

Conflict of interest

Jian CHEN, Yao KANG, Xudong WANG, Hao HUANG, and Man YAO declare that they have no conflict of interest.

References

Ahmed M, Li Y, Chen WC, et al., 2020. Diffusion barrier prediction of graphene and boron nitride for copper interconnects by deep learning. *IEEE Access*, 8:210542-210549. https://doi.org/10.1109/ACCESS.2020.3039257

Bahari Y, Mortazavi B, Rajabpour A, et al., 2021. Application of two-dimensional materials as anodes for rechargeable metal-ion batteries: a comprehensive perspective from density functional theory simulations. *Energy Storage Materials*, 35:203-282. https://doi.org/10.1016/j.ensm.2020.11.004

Blöchl PE, 1994. Projector augmented-wave method. *Physical Review B*, 50(24):17953-17979. https://doi.org/10.1103/PhysRevB.50.17953

Chaney G, Ibrahim A, Ersan F, et al., 2021. Comprehensive study of lithium adsorption and diffusion on janus Mo/W*XY* (*X*, *Y*=S, Se, Te) using first-principles and machine learning approaches. *ACS Applied Materials & Interfaces*, 13(30): 36388-36406. https://doi.org/10.1021/acsami.1c05508

Chang JH, Jørgensen PB, Loftager S, et al., 2021. On-the-fly assessment of diffusion barriers of disordered transition metal oxyfluorides using local descriptors. *Electrochimica Acta*, 388:138551. https://doi.org/10.1016/j.electacta.2021.138551

Chen C, Ye WK, Zuo YX, et al., 2019. Graph networks as a universal machine learning framework for molecules and crystals. *Chemistry of Materials*, 31(9):3564-3572. https://doi.org/10.1021/acs.chemmater.9b01294

Das S, Pegu H, Sahu KK, et al., 2020. 19-machine learning in materials modeling—fundamentals and the opportunities in 2D materials. *In*: Yang EH, Datta D, Ding JJ (Eds.), Synthesis, Modeling, and Characterization of 2D Materials, and Their Heterostructures. Elsevier, p.445-468. https://doi.org/10.1016/B978-0-12-818475-2.00019-2

Dong XC, Li HW, Jiang ZT, et al., 2021. 3D deep learning enables accurate layer mapping of 2D materials. *ACS Nano*, 15(2): 3139-3151. https://doi.org/10.1021/acsnano.0c09685

Dong Y, Wu CH, Zhang C, et al., 2019. Bandgap prediction by deep learning in configurationally hybridized graphene and boron nitride. *npj Computational Materials*, 5(1):26. https://doi.org/10.1038/s41524-019-0165-4

Giebeler L, Balach J, 2021. Mxenes in lithium–sulfur batteries: scratching the surface of a complex 2D material–a mini-review. *Materials Today Communications*, 27:102323. https://doi.org/10.1016/j.mtcomm.2021.102323

Grimme S, Antony J, Ehrlich S, et al., 2010. A consistent and accurate ab initio parametrization of density functional dispersion correction (DFT-D) for the 94 elements H-Pu. *The Journal of Chemical Physics*, 132(15):154104. https://doi.org/10.1063/1.3382344

Haastrup S, Strange M, Pandey M, et al., 2018. The computational 2D materials database: high-throughput modeling and discovery of atomically thin crystals. *2D Materials*, 5(4):042002. https://doi.org/10.1088/2053-1583/aacfc1

He KM, Zhang XY, Ren SQ, et al., 2016. Deep residual learning for image recognition. Proceedings of the IEEE Conference on Computer Vision and Pattern Recognition, p.770-778. https://doi.org/10.1109/CVPR.2016.90

Henkelman G, Jónsson H, 2000. Improved tangent estimate in the nudged elastic band method for finding minimum energy paths and saddle points. *The Journal of Chemical Physics*, 113(22):9978-9985. https://doi.org/10.1063/1.1323224

Huang G, Liu Z, van der Maaten L, et al., 2017. Densely connected convolutional networks. Proceedings of the IEEE Conference on Computer Vision and Pattern Recognition, p.2261-2269. https://doi.org/10.1109/CVPR.2017.243

Kabiraj A, Mahapatra S, 2022. High-throughput assessment of two-dimensional electrode materials for energy storage devices. *Cell Reports Physical Science*, 3(1): 100718. https://doi.org/10.1016/j.xcrp.2021.100718

Kang YQ, Li LJ, Li BH, 2021. Recent progress on discovery and properties prediction of energy materials: simple machine learning meets complex quantum chemistry. *Journal of Energy Chemistry*, 54:72-88. https://doi.org/10.1016/j.jechem.2020.05.044

Kresse G, Furthmüller J, 1996. Efficient iterative schemes for ab initio total-energy calculations using a plane-wave basis set. *Physical Review B*, 54(16):11169-11186. https://doi.org/10.1103/PhysRevB.54.11169

Langreth DC, Mehl MJ, 1983. Beyond the local-density approximation in calculations of ground-state electronic properties. *Physical Review B*, 28(4):1809-1834. https://doi.org/10.1103/PhysRevB.28.1809

Lee SJ, Theerthagiri J, Nithyadharseni P, et al., 2021. Heteroatom-doped graphene-based materials for sustainable energy applications: a review. *Renewable and Sustainable Energy Reviews*, 143:110849. https://doi.org/10.1016/j.rser.2021.110849

Leist C, He M, Liu X, et al., 2022. Deep-learning pipeline for statistical quantification of amorphous two-dimensional materials. *ACS Nano*, 16(12):20488-20496. https://doi.org/10.1021/acsnano.2c06807

Li WW, Ando Y, Minamitani E, et al., 2017. Study of Li atom diffusion in amorphous Li_3PO_4 with neural network potential. *The Journal of Chemical Physics*, 147(21):214106. https://doi.org/10.1063/1.4997242

Liu F, Fan ZX, 2023. Defect engineering of two-dimensional materials for advanced energy conversion and storage. *Chemical Society Reviews*, 52(5):1723-1772. https://doi.org/10.1039/D2CS00931E

Liu HP, Lei W, Tong ZM, et al., 2020. Defect engineering of 2D materials for electrochemical energy storage. *Advanced Materials Interfaces*, 7(15):2000494. https://doi.org/10.1002/admi.202000494

Liu Y, Wu JM, Avdeev M, et al., 2020. Multi-layer feature selection incorporating weighted score-based expert knowledge toward modeling materials with targeted properties. *Advanced Theory and Simulations*, 3(2):1900215. https://doi.org/10.1002/adts.201900215

Lu GM, Witman M, Agarwal S, et al., 2023. Explainable machine learning for hydrogen diffusion in metals and random binary alloys. *Physical Review Materials*, 7(10):105402. https://doi.org/10.1103/PhysRevMaterials.7.105402

Masubuchi S, Watanabe E, Seo Y, et al., 2020. Deep-learning-based image segmentation integrated with optical microscopy for automatically searching for two-dimensional materials. *npj 2D Materials and Applications*, 4(1):3. https://doi.org/10.1038/s41699-020-0137-z

Momma K, Izumi F, 2011. VESTA 3 for three-dimensional visualization of crystal, volumetric and morphology data. *Journal of Applied Crystallography*, 44(6):1272-1276. https://doi.org/10.1107/S0021889811038970

Paszke A, Gross S, Massa F, et al., 2019. PyTorch: an imperative style, high-performance deep learning library. *In*: Wallach H, Larochelle H, Beygelzimer A (Eds.), Advances

in Neural Information Processing Systems, 32. Curran Associates, p.8024-8035.

Perdew JP, Burke K, Ernzerhof M, 1996. Generalized gradient approximation made simple. *Physical Review Letters*, 77(18):3865-3868. https://doi.org/10.1103/PhysRevLett.77.3865

Ryu B, Wang LQ, Pu HH, et al., 2022. Understanding, discovery, and synthesis of 2D materials enabled by machine learning. *Chemical Society Reviews*, 51(6):1899-1925. https://doi.org/10.1039/D1CS00503K

Sendek AD, Yang Q, Cubuk ED, et al., 2017. Holistic computational structure screening of more than 12000 candidates for solid lithium-ion conductor materials. *Energy & Environmental Science*, 10(1):306-320. https://doi.org/10.1039/C6EE02697D

Shao QJ, Wu ZS, Chen J, 2019. Two-dimensional materials for advanced Li-S batteries. *Energy Storage Materials*, 22:284-310. https://doi.org/10.1016/j.ensm.2019.02.001

Simonyan K, Zisserman A, 2014. Very deep convolutional networks for large-scale image recognition. arXiv:1409.1556. https://doi.org/10.48550/arXiv.1409.1556

Tan CQ, Sun FC, Kong T, et al., 2018. A survey on deep transfer learning. The 27th International Conference on Artificial Neural Networks and Machine Learning, p.270-279. https://doi.org/10.1007/978-3-030-01424-7_27

Theerthagiri J, Lee SJ, Karuppasamy K, et al., 2021. Application of advanced materials in sonophotocatalytic processes for the remediation of environmental pollutants. *Journal of Hazardous Materials*, 412:125245. https://doi.org/10.1016/j.jhazmat.2021.125245

Theerthagiri J, Park J, Das HT, et al., 2022a. Electrocatalytic conversion of nitrate waste into ammonia: a review. *Environmental Chemistry Letters*, 20(5):2929-2949. https://doi.org/10.1007/s10311-022-01469-y

Theerthagiri J, Karuppasamy K, Lee SJ, et al., 2022b. Fundamentals and comprehensive insights on pulsed laser synthesis of advanced materials for diverse photo- and electrocatalytic applications. *Light: Science & Applications*, 11(1):250. https://doi.org/10.1038/s41377-022-00904-7

Wang GY, Fearn T, Wang TY, et al., 2021. Machine-learning approach for predicting the discharging capacities of doped lithium nickel–cobalt–manganese cathode materials in Li-ion batteries. *ACS Central Science*, 7(9):1551-1560. https://doi.org/10.1021/acscentsci.1c00611

Wang RH, Li MH, Sun KW, et al., 2022. Element-doped mxenes: mechanism, synthesis, and applications. *Small*, 18(25): 2201740. https://doi.org/10.1002/smll.202201740

Wang XG, Meng LJ, Li BX, et al., 2021. Heteroatoms/molecules to tune the properties of 2D materials. *Materials Today*, 47:108-130. https://doi.org/10.1016/j.mattod.2020.12.019

Wang XL, Xiao RJ, Li H, et al., 2017. Quantitative structure-property relationship study of cathode volume changes in lithium ion batteries using ab-initio and partial least squares analysis. *Journal of Materiomics*, 3(3):178-183. https://doi.org/10.1016/j.jmat.2017.02.002

Wu Y, Yu Y, 2019. 2D material as anode for sodium ion batteries: recent progress and perspectives. *Energy Storage Materials*, 16:323-343. https://doi.org/10.1016/j.ensm.2018.05.026

Xie T, Grossman JC, 2018. Crystal graph convolutional neural networks for an accurate and interpretable prediction of material properties. *Physical Review Letters*, 120(14): 145301. https://doi.org/10.1103/PhysRevLett.120.145301

Yosinski J, Clune J, Bengio Y, et al., 2014. How transferable are features in deep neural networks? Proceedings of the 28th International Conference on Neural Information Processing Systems, Volume 2, p.3320-3328.

Zhan C, Sun WW, Xie Y, et al., 2019. Computational discovery and design of mxenes for energy applications: status, successes, and opportunities. *ACS Applied Materials & Interfaces*, 11(28):24885-24905. https://doi.org/10.1021/acsami.9b00439

Zhang WS, Liu SY, Chen J, et al., 2021. Exploring the potentials of $Ti_3C_iN_{2-i}T_x$ (i=0, 1, 2)-mxene for anode materials of high-performance sodium-ion batteries. *ACS Applied Materials & Interfaces*, 13(19):22341-22350. https://doi.org/10.1021/acsami.1c02470

Zhang XY, Zhou J, Lu J, et al., 2022. Interpretable learning of voltage for electrode design of multivalent metal-ion batteries. *npj Computational Materials*, 8(1):175. https://doi.org/10.1038/s41524-022-00858-9

Zhang YQ, Tao L, Xie C, et al., 2020. Defect engineering on electrode materials for rechargeable batteries. *Advanced Materials*, 32(7):1905923. https://doi.org/10.1002/adma.201905923

Electronic supplementary materials

Figs. S1–S9, Table S1, Eqs. (S1)–(S4)